Journal of The Electrochemical Society

The Electrochemical Society
Advancing solid state & electrochemical science & technology

OPEN ACCESS

Non-Destructive Detection of Local Aging in Lithium-Ion Pouch Cells by Multi-Directional Laser Scanning

To cite this article: Johannes Sturm *et al* 2017 *J. Electrochem. Soc.* **164** A1342

View the article online for updates and enhancements.

This content was downloaded from IP address 138.246.3.249 on 02/08/2021 at 09:04

Non-Destructive Detection of Local Aging in Lithium-Ion Pouch Cells by Multi-Directional Laser Scanning

Johannes Sturm,*,z F. B. Spingler, B. Rieger,* A. Rheinfeld,* and Andreas Jossen

Technical University of Munich, Institute for Electrical Energy Storage Technology, Munich, Germany

Understanding the mechanical activity of lithium-ion cells during cycling and its connection with aging phenomena is essential to improve cell design and operation strategies. Previous studies of lithium-ion pouch cells [B. Rieger et al., *Journal of Energy Storage*, **8**, 1 (2016)] have shown non-uniform swelling with local displacement overshoots during charging. In this experimental work, a novel three-dimensional laser scanning method is used to investigate local reversible and irreversible thickness changes of six commercial $LiCoO_2$/graphite cells during a cyclic aging experiment. Three cycle scenarios were included and two cells each were exposed to a specific temperature and charging rate. The cells showing local displacement overshoots also exhibit non-uniform distributions of irreversible thickness change. Post-mortem analysis showed largely inhomogenously degraded surfaces of the single anode layers. It is shown that the cells' irreversible thickness change correlates with capacity fade and internal resistance increase monitored via electrochemical impedance spectroscopy.

© The Author(s) 2017. Published by ECS. This is an open access article distributed under the terms of the Creative Commons Attribution 4.0 License (CC BY, http://creativecommons.org/licenses/by/4.0/), which permits unrestricted reuse of the work in any medium, provided the original work is properly cited. [DOI: 10.1149/2.0161707jes] All rights reserved.

Manuscript submitted March 9, 2017; revised manuscript received April 11, 2017. Published April 29, 2017.

Lithium-ion batteries have become the most promising energy storage technology for small electronic devices such as smartphones or laptops as well as for battery packs in electric vehicles. Although their relatively high density in power and energy make Li-ion batteries the technology of choice for many applications, its aging and degradation behavior likewise limits their use in applications that require extreme safety standards and cycle life.[2] In order to quantify the decay of batteries, the *state of health* (SOH)[3] is used which refers to the capacity fade by relating the current capacity of the cell to its initial capacity. This relation can be seen as an overall concept introducing a measurable quantity of aging effects occurring during battery lifetime.

Detecting the cell's SOH by measuring external stress and strain on the surface of the cell's housing[2,4] is a recent method based on the mechanical behavior of Li-ion batteries in form of volume change effects during charge and discharge processes. These are largely caused by electrode swelling,[5–8] polymer deformation[5,9] and film growth.[10,11]

Estimating the cell's SOH by a single point measurement implies a homogeneous stress and strain distribution over the housing of the cell. Hence, the utilization of the cell would need to be homogeneous. Local variations in current density and electrode potential occurring during cell operation along the current collector foils[12–15] object this assumption. Considering an inhomogeneous utilization of the electrodes described by local variations in *state of charge* (SOC),[15] an overall estimation of SOH seems inappropriate to gain a deeper understanding of aging mechanisms occurring in commercial Li-ion cells. Consequently, there is a need for local detection of aging mechanisms to account for design specific inhomogeneous load across the cell.

As already presented in previous work,[1] extending the measurement of strain or stress to a local resolution allows for local analysis of lithium-ion cell aging. This information may provide a more profound data basis for explaining displacement overshoots near the end of the charging process under constant current which were described in detail in several previous works[1,7,16] and were ascribed to failure mechanisms.

Continuous analysis of cell aging during cycling requires an appropriate method which is able to monitor the local state of the cell without damaging it. For analyzing local aging effects, post-mortem analysis such as disassembling methods enable to investigate local degradation phenomena but are cost and time consuming.[17–19]

Beside non-destructive methods such as electrochemical impedance spectroscopy (EIS),[20] differential voltage analysis (DVA)[21] or neutron diffraction (ND),[22–25] measuring the cell's thickness proved to be a reliable method for determining intercalation stages in the electrodes[7,26,27] and the corresponding electrode specific SOC, to monitor irreversible swelling effects during aging[4] and to detect lithium plating.[16,28] ND[22–25] is not readily available as the experimental setup is highly complex and expensive which makes it inappropriate in our case. Even though EIS and DVA are frequently used to describe overall cell aging,[29–31] these characterization methods do not provide information about local cell aging.

Placing tactile high precision fiber optic sensors on the cell's surface is challenging due to space restrictions, only a few positions[6–8,32,33] can be measured simultaneously. In another work[16] a single tactile dial-indicator was placed on the surface of a lithium-ion cell in order to investigate the formation of lithium plating. However, the measurements only considered a single measurement point assuming a homogeneous distribution of the formed deposit layer. The work of Birkenmaier et al.[28] dealt with the detection of the spatial distribution of lithium plating by point-laser sensor measurements. Measurements are gathered from one side of the cell requiring an initial data set in order to correct the recorded thicknesses at each point. Hence process time increase and displacement results are always dependent on the initial state.

The multidirectional laser scanning technique described in our previous work[1] combines several advantages compared to the measurement methods mentioned above. This method provides an in-operando, non-destructive measurement and the variable number of measurement points ensures an adequate covering of the entire cell-stack related surface area of the cell. Owing to the application of linear laser sensors placed on both sides of the cell, no correction referring to the initial state of the recorded thicknesses has to be performed which reduces the effort in post-processing and ensures robustness toward spatial displacements of the whole cell within the measurement area.

Experimental

Experimental setup.—Six 2.28 Ah Enertech SPB655060 pouch cells with a $LiCoO_2$/graphite cell chemistry were used for the cyclic aging experiments. In Table I, the basic parameters of the studied cell are outlined. More detailed electrode and cell data are provided in our previous work.[26]

In a previous study of the same cell,[1] an overshoot in the thickness change near the tabs was observed at a 1 C charging rate and 25°C chamber temperature, which was not observed anymore when the temperature was increased to 40°C. To investigate the impact of this phenomenon on reversible and irreversible thickness change as well as capacity fade and impedance response, three cycling scenarios were chosen for the experiments. Six cells were considered, two cells

*Electrochemical Society Student Member.
zE-mail: johannes.sturm@tum.de

Table I. Enertech SPB655060 pouch cell specifications.[26]

Name	Value
Capacity	2.28 Ah
Maximum charging rate	1 C
Maximum discharging rate	2 C
Cell length	60 mm
Cell width	50 mm
Cell height	6.4 mm
Anode electrode length	52 mm
Cathode electrode length	51 mm
Anode electrode width	46.4 mm
Cathode electrode width	45.4 mm
Anode coating thickness	77 ± 0.5 µm
Cathode coating thickness	68 ± 0.5 µm
Double-coated anode layers	17
Double-coated cathode layers	16
Single-coated cathode layers	2

Table II. Cycling conditions for the studied cells.

Cell	Charging rate	Temperature	Displ. overshoot
#80	0.5 C	25°C	no
#82	0.5 C	25°C	no
#83	1 C	25°C	yes
#84	1 C	25°C	yes
#85	1 C	40°C	no
#86	1 C	40°C	no

each were exposed to a specific combination of charging rate and cell temperature. The cycling conditions for each pair of cells are shown in Table II. The scenarios with 0.5 C charging rate at 25°C and 1 C charging rate at 40°C are denoted as *homogeneous* charging scenarios, as the displacement during charging was uniform across the cell and no local overshoot was observed.[1] The scenario with 1 C charging rate at 25°C is denoted as *inhomogeneous* charging, as a displacement overshoot was observed near the tabs.[1]

The same discharge rate was used for all cells to assure that the observed effects are caused by either charging rate or temperature. The detailed experimental procedure for cycling and check-up are given in Table III. Cycling was conducted inside a temperature chamber. Every 100 cycles, the cell was charged to 100% SOC and left for relaxation for at least 20 h to assure reliable impedance measurements.[34] The impedance was measured at 25°C using a VMP3 potentiostat (Bio-

Table III. Procedure for cycling and check-up.

Parameter	Value
Cycling	
Charging rate	see Table II
Temperature	see Table II
Charge	CC to 4.2 V - CV until I<0.1 C
Pause	30 min
Discharge	1 C CC to 3.0 V
Pause	30 min
Check-up	
Charge	0.5 C CC to 4.2 V - CV until I<0.05 C
Pause	20 h
Location	Temperature chamber at 25°C
EIS	100 kHz to 45 mHz
Location	Laser test bench at 25°C
Discharge	0.5 C CC to 3.0 V - CV until I<0.05 C
Pause	30 min
Charge	0.1 C CC to 4.2 V - CV until I<0.05 C
Pause	30 min
Discharge	0.1 C CC to 3.0 V - CV until I<0.05 C

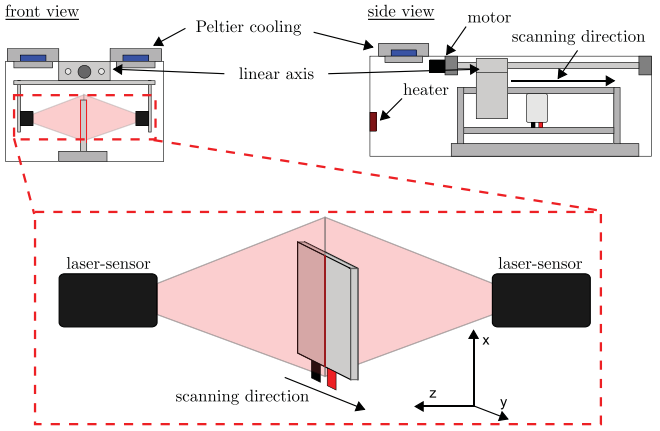

Figure 1. Experimental structure of the laser test bench.

Logic SAS, France). Next, a laser check-up to detect the local reversible and irreversible thickness changes of the cell was conducted. In Fig. 1 the structure of the laser test bench is shown. The procedure in the laser test bench was repeated up to five times depending on the capacity fade of the respective cell. The scanning process caused no heat generation on the cell itself and the cell behavior was therefore not influenced by the measurement equipement. For the check-up inside the laser test bench, which was also kept at 25°C, the local thickness of the cell at 99 positions was recorded every 60 s during the full cycle at 0.1 C charging and discharging rate. This cycle at low current also serves for the capacity measurement and differential voltage analysis.

The reversible thickness change was measured between the fully charged and fully discharged state. At the end of this phase the irreversible thickness change of the cell was detected. A calibration of the laser test bench was conducted before every check-up by using a calibration bar, and preliminary experiments showed that the resulting uncertainty at a given position is no more than ±5 µm for a single measuring process, which is much smaller than displacement effects during cycling. For further information about the two test environments and the post processing procedure, the reader is referred to our previous work.[1]

Mechanical activity of lithium-ion cells.—There are several works dealing with the absolute thickness change of cells during charging and discharging based on temperature effects, intercalation stages within the electrodes as well as mechanical inhomogeneities in cells.[22,35,36]

The effect of thermal expansion is negligible in the present study, as the thickness measurement is conducted at a low current rate of 0.1 C, leading to a thermal expansion which is below the laser scanner resolution.[1]

The intercalation induced volume expansion within the graphite electrode was estimated to more than 10%,[67] referring to the fully deintercalated state. However, the deintercalation induced volume expansion of $LiCO_2$ electrodes was determined to be around 2.3%[67], referring to the fully intercalated state. More information about the intercalation induced volume expansion is given in previous work[67]. The intercalation induced thickness change of lithium-ion cells is strongly related to intercalation stages of lithium in graphite.[6,26,27] As the lithiation degree of graphite changes with aging,[22,23] a variation of the reversible thickness change is expected. The reversible thickness change $\triangle t_{rev}$ induced by intercalation and deintercalation[26] can be defined as follows:

$$\triangle t_{rev} = t_{cell,SOC=1,k} - t_{cell,SOC=0,k} \quad [1]$$

For a check-up after cycle quantity k, the reversible thickness change is derived from the local thickness values between fully charged (SOC = 1) and completely discharged (SOC = 0) state of the cell, see Fig. 2.

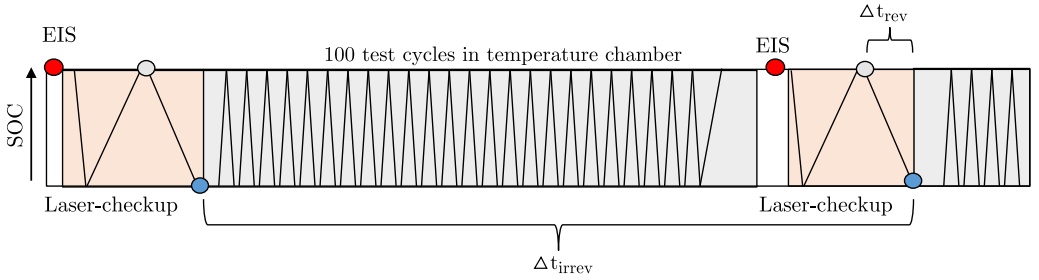

Figure 2. Cycling procedure in the aging experiment. After every 100 cycles in the temperature chamber, an EIS and a check-up is performed via laser scanning to determine the irreversible and reversible thickness change.

The irreversible part of the thickness change can be related to solid electrolyte interphase (SEI) growth[37] in the form of a deposit layer on the particles of the graphite electrode, new crystal arrangement within the particles,[38] increasing porosity of the electrodes due to continuous volume change[39] as well as particle size increase caused by void formation.[40] The parameter $\triangle t_{irrev}$ is determined by subtracting the initial thickness ($k = 0$) from the thickness at the end of check-up after cycle quantity k. Both thickness values are measured in the fully discharged state of the cell (SOC = 0).

$$\triangle t_{irrev} = t_{cell,SOC=0,k} - t_{cell,SOC=0,k=0} \quad [2]$$

In addition to the causes mentioned above for reversible and irreversible thickness changes, lithium plating at the graphite anode needs to be considered.[16,24] Lithium plating describes the precipitation of metallic lithium on the surface of the solid particles. This deposit layer causes a higher volume change than intercalation into the host lattice.[41,42] This process is partly reversible as some of the plated lithium intercalates after the charging process is finished.[24] The lithium remaining on the surface is considered to be irreversibly deposited.[37,43] The irreversibly deposited lithium causes a permanent thickness change.[16,28] Experimental measurements in the work of Agubra et al.[37] determined the irreversible thickness change per electrode layer to be between 21 µm and 53 µm depending on the local SOC and the affected area of the anode. These measurements were gained from an accelerated aging cycle (4 C) involving 600 cycles applied to a NMC/graphite pouch cell which was analyzed by means of a destructive post-mortem method. In another work of Agubra et al.,[43] the same cell was subjected to 600 cycles at different current rates (2 C, 3 C, 4 C) and the irreversible thickness change was determined to range from 1 µm to 37 µm for 2 C and from 27 µm to 56 µm for 4 C. This supports the assumption that higher charging rates result in a stronger formation of deposit layers at the anode.[44] Burow et al.[45] analyzed the formation of plated lithium for the same cell chemistry in a prismatic cell format. Using an accelerated aging process via pulse charging (8 C), the irreversible thickness increment was determined to range from 11 µm to 31 µm for a single anode sheet after 500 cycles in a post-mortem analysis.

In the work presented here, the investigation of local reversible and irreversible thickness changes under the aforementioned homogeneous and inhomogeneous charging scenarios is investigated by using a novel 3D laser scanning characterization method.

Correlation of aging effects.—As introduced in another work,[46] EIS can be a helpful tool for characterization of aging effects, such as SEI. The formation of SEI is caused by irreversible electrochemical decomposition of the electrolyte at the surface of the active material particles.[10] The growth of SEI implies a certain loss of cycleable lithium[11,30] and the additional layer causes a rising resistance of the cell.[11,47] The increment of internal resistance can be detected by EIS[48] in the form of impedance buildup during aging. In this work, EIS data of the cycled cells at 1 kHz and 45 mHz were analyzed to quantify the growth of pure ohmic and DC-resistance, respectively.

Recent research deals with the estimation of SOC[49] and SOH/capacity fade[4,50] by measuring the pressure evolution in mechanically restricted cells. Considering homogeneous aging behavior of the cell, a linear dependency between the measured pressure and SOH was found, which does not hold for strongly aged cells.[9] In continuation of these studies, this work focuses on the correlation of internal resistance, irreversible thickness change and capacity fade.

Results and Discussion

Firstly, the capacity fade during the cyclic aging tests is discussed. Further on, the reversible and irreversible thickness changes are analyzed and the correlation between displacement, capacity fade and internal resistance is investigated. Finally, the observed capacity fade is correlated to the DVA-results to identify electrode specific degradation.

Capacity fade.—During each check-up phase, the capacity of the cells was determined according to Table III. In Fig. 3 the capacity fade is shown as a function of cycle number for all studied cells. The capacities are normalized to their initial state (fresh cell). The results indicate a nearly linear decrease of capacity with growing cycle number for the cells which showed no displacement overshoot (see Table II). The cells showing a local overshoot in displacement are characterized by a distinct capacity loss of up to 30% and 40% at cycle number 230 and 396, respectively. The significant decay of these cells points at a distinct aging process which will be further analyzed in the following chapters.

Spatial distribution of reversible and irreversible thickness changes.—The development of the local reversible thickness change from the initial state to 500 cycles is shown in Fig. 4 for cell #80. At the beginning of the cycling experiment, no significant displacement inhomogeneities were detected across the cell. The average reversible thickness change between discharged and charged state was about 160 µm. From 100 to 500 cycles, however, a greater reversible thickness change could be found near the edges of the cell. It was shown in previous works[28,36] that lithium plating initiates in areas close to the edges of the electrodes due to manufacturing tolerances and edge effects. Furthermore, ND analysis showed an accelerated aging behavior

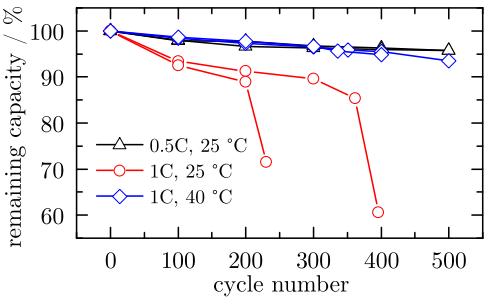

Figure 3. Capacity fade of the six cells considered in this aging experiment.

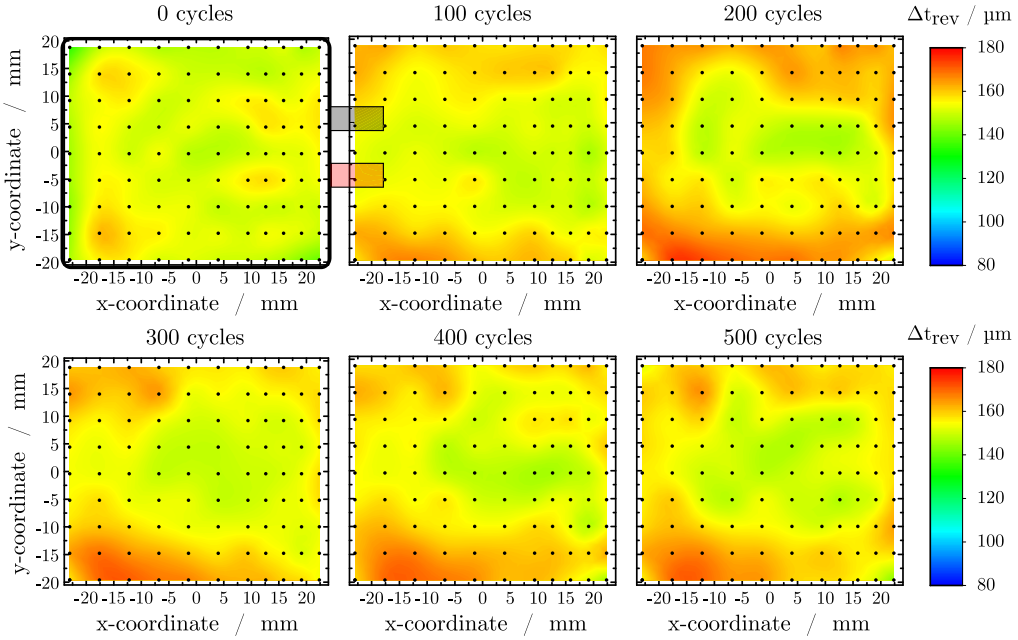

Figure 4. Development of the local reversible thickness change Δt_{rev} for a cell cycled at a charging rate of 0.5 C at 25°C (#80). The 99 measurement points of the laser sensors are denoted by the black dots within each depicted surface plot.

in these regions.[22] Bearing in mind these observations and accounting for a stronger fixation of the electrode stack near the edges due to the seam of the pouch-foil, the higher reversible thickness change seems to be justifiable. The mean value of Δt_{rev} was estimated to be 160 µm in our previous work[1] which is in good agreement with the values presented in this work. The irreversible thickness changes for cell #80 upon cycling are shown in Fig. 5. The thickness of the cell increased continuously without the occurrence of distinct inhomogeneities. Within the first 100 cycles, the irreversible thickness increase was around 50 µm. The following check-ups showed a lower increase of approximately 30 µm per 100 cycles with a final displacement of about 140 µm after 500 cycles. The irreversible thickness increase is expected to be caused by swelling of polymer components such as separator and binder in the electrodes[51] as well as SEI growth, and was therefore mainly attributed to the anode in previous publications.[4,52,53] Gas evolution may also be a contributing factor to the overall thickness change as CO_2-gas evolves during cycling.[54] However, based on the thickness change during cycling of a punctured and a gastight pouch cell, Cannarella et al.[4] state that the effect of gas evolution on irreversible thickness change can be neglected. The second cell (#81) cycled at a charging rate of 0.5 C at 25°C showed nearly the same behavior for reversible and irreversible thickness change.

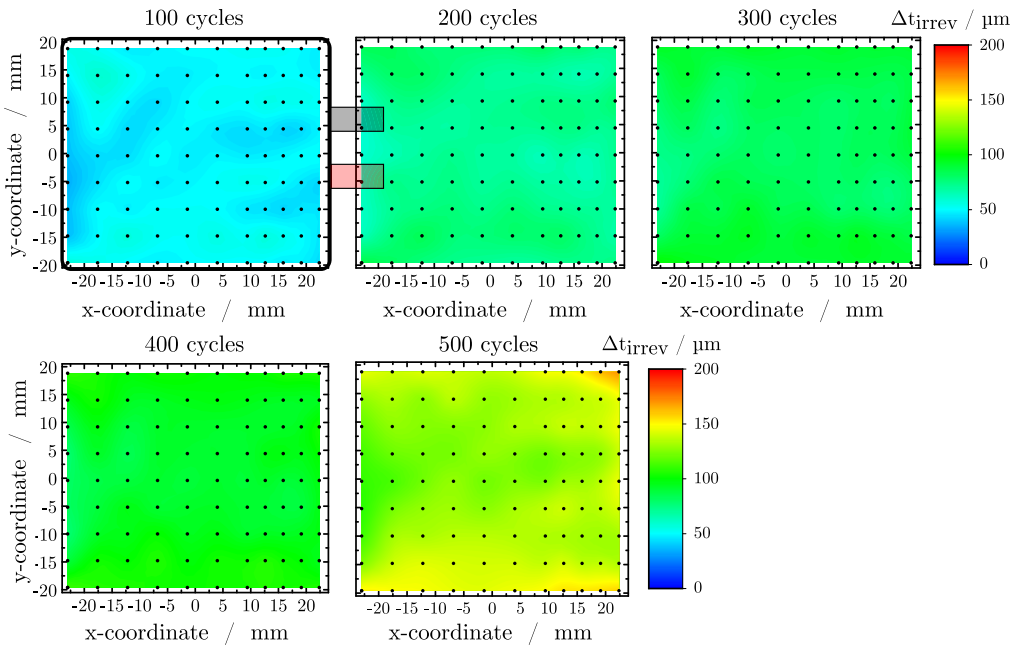

Figure 5. Development of the local irreversible thickness change Δt_{irrev} for a cell cycled at a charging rate of 0.5 C at 25°C (#80). The check-up results at cycle 0 are not shown here because no significant irreversible thickness changes could be detected.

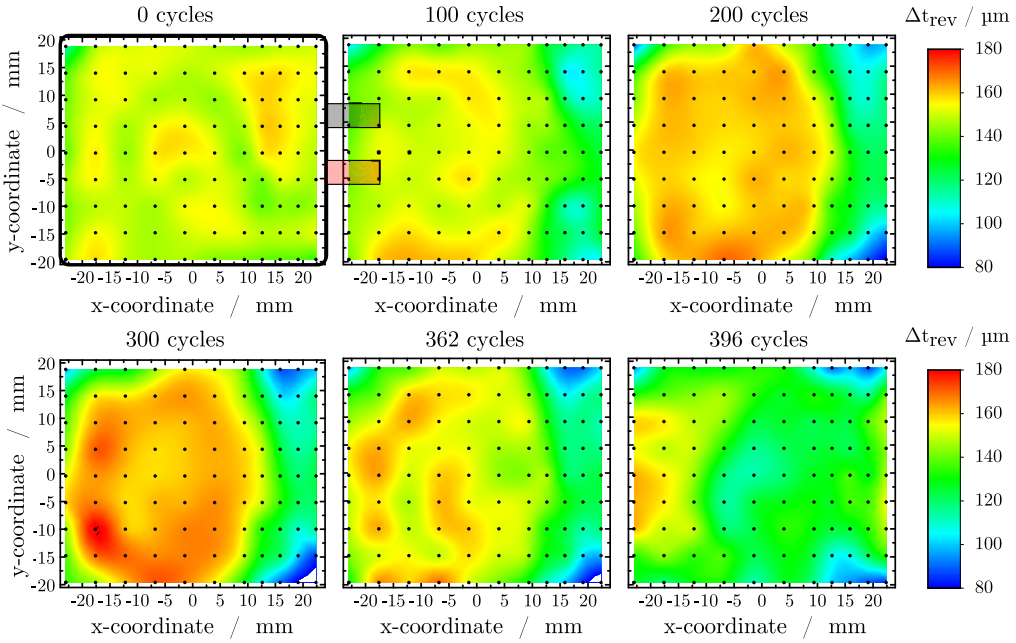

Figure 6. Development of the local reversible thickness change Δt_{rev} for the cell cycled at a charging rate of 1 C at 25°C with longer cycle life (#83).

The cells cycled at a charging rate of 1 C and 40°C showed similar behavior to the cells cycled at a charging rate of 0.5 at 25°C and are not discussed in detail here.

At a charging rate of 1 C at 25°C, not only severe capacity fade was observed at cycle 230 and 396 (see Fig. 3) but also distinct inhomogeneities in reversible and irreversible thickness change appeared in cells showing a displacement overshoot. In the following, the local reversible and irreversible thickness changes of cell #83 cycled at a charging rate of 1 C at 25°C are presented and discussed. The authors choosed this cell due to the longer cycle life compared to cell #84 and because both cells showed very similar reversible and irreversible thickness changes in the cyclic aging experiment.

The local reversible thickness change of cell #83 is presented in Fig. 6. Initially, the cell showed a rather homogeneous reversible displacement. In contrast to the cells cycled at 40°C and at a charging rate of 0.5 C at 25°C, a lower reversible displacement in the area near the tabs could be observed after 100 cycles. This phenomenon may indicate that the electrode's active material is damaged. With increasing cycle number, the magnitude in reversible displacement remained nearly constant in this specific area whereas it reached higher values in the other parts of the cell. These observations led to the conclusion that the undamaged areas of the cell were more utilized. This non-linear aging behavior was investigated in more detail between the 362nd and the 396th cycle. For this purpose, the cycling procedure in the climate chamber was interrupted in order to perform 34 cycles inside the laser chamber with simultaneous thickness measurement. Regarding the difference between the results of the check-ups after the 362nd and the 396th cycle, the formerly pronounced reversible thickness change in the area opposite to the tabs decreased while close to the tabs no significant changes were seen. The decreasing reversible thickness changes at cycle 396 may also refer to the distinct capacity fade at cycle 396 (see Fig. 3) which is linked to a certain loss of cycleable lithium. Consequently the lithiation range of both electrodes during a full cycle is narrowed and the overall reversible cell displacement, which is directly related to the lithiation stages of the electrodes, is reduced in the same amount. Again, the reader is referred to the work of Rieger et al.[67] for more information about the lithiation induced volume change of the $LiCO_2$/graphite electrodes.

The irreversible thickness changes of cell #83 are shown in Fig. 7. An increased irreversible thickness change could be observed in the area close to the tabs after 100 cycles. The mean irreversible thickness increase of around 300 µm in this region was even higher than the largest irreversible thickness change after 500 cycles of the cells cycled at 40°C and at a charging rate of 0.5 C at 25°C. The remaining cell area showed an irreversible thickness increase which is comparable to cells operated at a 0.5 C charging rate at the same temperature (#80 and #82). After 200 cycles, the irreversible thickness change near the tabs reached values of up to 500 µm whereas the remaining cell area only showed a moderate increase of around 100 µm. The irreversible thickness changes for 300 cycles indicated no significant degradation in the major part of the cell but after 362 cycles an enormous increase was detected. The damaging effect took place also in the remaining part and after 396 cycles displacements of up to 1500 µm were seen.

Comparing the local reversible and irreversible thickness changes, it seems that larger reversible thickness changes in a given area lead to larger irreversible thickness change in the same area. At first, the area close to the tabs showed as large reversible thickness changes as the center part of the cell, probably due to relatively low ohmic losses and resulting good utilization of the active material.[12,15,55] For all follwing check-ups, however, decreasing local reversible thickness change resulted in larger irreversible thickness increase in the area near to the tabs. The lower reversible thickness change indicates a lower utilization and perhaps that the material is damaged, which is in agreement with the dramatic increase in irreversible thickness change shown in Fig. 7. Interestingly, this is followed by an onset of large reversible thickness changes in the center of the cell at cycle 200 and 300, respectively, which may indicate that these areas compensate for the damaged material close to the tabs. At cycle 362, in a similar way to the area close to the tabs, reversible thickness change of the center area decreased while irreversible thickness change increased dramatically. This trend culminated at cycle 396, where most of the cell area showed relatively small reversible thickness changes and the irreversible thickness change reached values of up to 1500 µm. At this point, the SOH of the cell was as low as 60%. Considering these large irreversible thickness increases, lithium plating may play a major role in this process, which is in line with the severe capacity fade[45,47] of these cells, see Fig. 3. This raises the question how utilization and lithium plating are connected. Generally, a high local utilization is equivalent to a high current density of lithium ions. This leads to

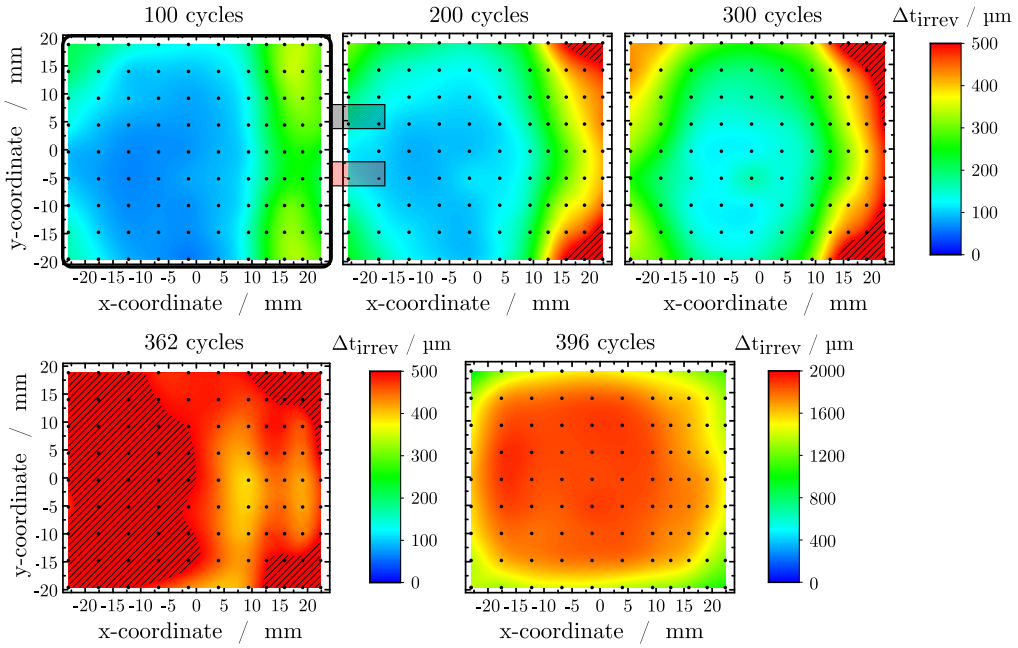

Figure 7. Development of local irreversible thickness changes Δt_{irrev} for the cell cycled at a charging rate of 1 C at 25°C with longer cycle life (#83).

high overpotentials in the anode which, during charging, may promote lithium plating to a certain extent.[16,56,57]

Cell #84, which showed a steeper capacity decrease in the inhomogeneous charging scenario, was opened for measuring the thickness of the individual electrodes. Each double side coated anode sheet showed a deposit layer on both sides resulting in a thickness increase ranging between 15 and 40 µm on each side which was measured by using a micrometer screw. These values are comparable to findings by other groups.[37,43,45] The sum of the thicknesses of all deposit layers on the 34 anode sheets agrees with the observed overall thickness increase of the cell. Regarding the irreversible thickness changes from cycle number 362 to 396, the mean value across the measurement area was found to be 1.0911 mm which translates into a relative thickness increase of 17% for the whole cell. The active area of the cell is restricted to the dimensions of the double side coated cathode sheet as it is the smaller one of the two electrodes (see Table I). Considering a corresponding active area of 2315.4 mm^2, a total volume change of 2526.33 mm^3 was determined. The total loss of capacity between the 362nd and 396th cycle amounts to 0.5768 Ah. Considering a molar volume of 13.1 $cm^3\ mol^{-1}$ of metallic lithium,[58] the volume of the lost cycleable lithium inventory when in the metallic state is estimated to be 281.93 mm^3. The measured volume change, however, is approximately 9 times larger. But it is unlikely that the plated lithium forms a homogeneous layer. The deviation may be explained by mossy and dendritic deposition of lithium, which takes up more volume than a film of solid lithium.[28,59] In order to validate this assumption, a post-mortem analysis of cell #83 was conducted to investigate possible damages on the electrode sheets. As shown in Fig 8, anode sheets were largely covered with inhomogeneously distributed deposit layers. It may be assumed that these mossy layers of all anode sheets combined caused the greater part of the enormous thickness increase. On the cathode sheets no deposit layer or other damages could be seen directly. Severe inhomogeneously distributed deposit layers could be seen on every anode layer and no significant differences were found between the 17 sheets. In summary, prominent mossy deposit layers were observed on the anode, however, there is no clear proof that they correlate with the amount of lost cycleable lithium.

Breaking down the thickness increment per single sided anode sheet from the full cell measurement, each of the 34 coated layers would have grown by 32.1 µm within the last 34 cycles. This corresponds to a growth of 41.7% of the coating thickness. The overall thickness change per layer between the cell's initial state prior to the applied cycling procedure and its final state after cycling can be found to be 47.3 µm which corresponds to a relative thickness increase of 61.4%. In the work of Burow et al.,[45] the initial layer thickness of the graphite coated copper foil was 60 µm and the minimal thickness increase was 51.7% since the thickness of the copper foil is unknown here. Gallagher et al.[60] estimated the increase for 58 µm and 97 µm initial coating thickness to be 12.1% and 72.2%, respectively. Comparing our results with these works, the relative increase seems justifiable.

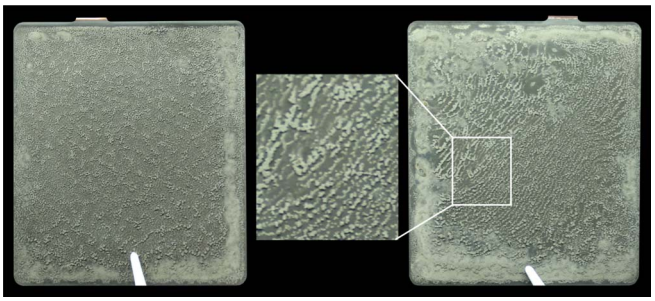

Figure 8. Deposit layers on both sides of the graphite anode of cell #83 after opening in an argon filled glove box. The inhomogeneous structure of the deposit layers is shown in the magnified area. The tweezers used for clamping the sheets are visible at the bottom of the picture.

Correlation of capacity fade, thickness increase and impedance data.—The measurements of capacity fade, irreversible thickness change and impedance of the studied cells are shown in Fig. 9 for all check-ups. The depicted values are normalized to the initial state of the check-up at 0 cycles. The irreversible thickness change is derived as a mean value from the 99 measured points distributed across the surface area of each cell. At cycle 230 and 396 in Fig. 9b, the excessive increase of irreversible thickness change up to 20% and 25% was subjected to the cells cycled at a charging rate of 1 C at 25°C,

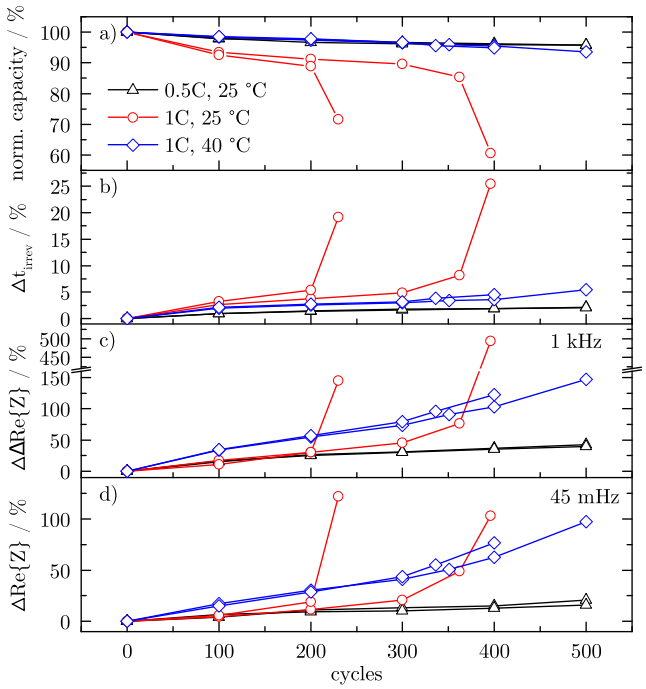

Figure 9. Comparison of a) normalized capacity fade, b) mean irreversible cell thickness change and normalized impedance rise at c) 1 kHz and at d) 45 mHz.

respectively. During the whole aging test in this study, a steeper increase and higher values of the irreversible thickness change for these cells were found compared to the remaining four cells. At a charging rate of 1 C at 40°C both cells showed irreversible thickness changes from 3% up to 5% after 400 cycles. The measurements of the cells at a charging rate of 0.5 C at 25°C exhibited the lowest irreversible thickness changes (2%) of all studied cells.

Comparing Fig. 9a to Fig. 9b, a correlation between normalized capacity loss and irreversible thickness increase may be assumed for all cells. The higher the capacity fade, the higher the irreversible thickness change. The rapid increase of capacity fade between the last two check-ups (200^{th}/230^{th} and 362^{th}/396^{th}) of the cells cycled at a charging rate of 1 C at 25°C is comparable to the findings of other researchers for cylindrical cells.[29,47] In this context the correlation has been denoted as non-linear aging effect. The correlated excessive thickness increase in Fig. 9b confirms the assumed correlation for these cells. None of the cells cycled at a charging rate of 0.5 C at 25°C and 1 C at 40°C showed such a non-linear behavior in this study. The difference between these cells exhibited a higher capacity fade and a greater irreversible thickness increase for the latter ones. This may reveal a certain charging rate or temperature influence which was not investigated in further detail here.

The real parts of the measured cell impedances are shown in Figs. 9c and 9d for a high (1 kHz) and a low (45 mHz) excitation frequency, respectively. At cycle 100 and 200 in Fig. 9c, the values for the impedance rise at 1 kHz exhibit no significant differences for the four cells cycled at 25°C and were estimated to be around 10%. At this point, both cells cycled at 40°C already showed an increase of up to 30%. At cycle 230, the last check-up of one cell (#84) cycled at a charging rate of 1 C at 25°C revealed an excessive impedance increase up to 150%. The second cell (#83) of this charging scenario, showed a steeper impedance rise after cycle 300 and 362 compared to the two cells cycled at a charging rate of 0.5 C at 25°C. Again at cycle 396, this cell (#83) revealed an excessive impedance rise of 500% at 1 kHz. The impedance of the cells cycled at 0.5 C at 25°C was steadily increasing by up to 45% at cycle 500 without an excessive increase during the whole aging test. The final impedance rises for the cells cycled at a charging rate of 1 C at 40°C were estimated to be 125% and 150% at cycle 400 and 500, respectively.

All studied cells show a distinct increase of the measured impedance for increasing cycle number which can be related to the formation of a SEI-layer.[10] Steeper impedance rise of the cells cycled at 40°C compared to the cells cycled at 25°C may be related to an accelerated SEI growth at higher temperatures for both excitation frequencies.[61] The cells cycled at a charging rate of 1 C at 25°C show excessive impedance rise at the final check-ups which probably may not be justified by SEI-growth alone. The authors conclude, that the greater part is caused by the progressive loss of lithium due to the formation of deposit layers which correlates with the increasing mean irreversible thickness change of the cell at the same time (see Fig. 9b).

As seen in Fig. 9c until cycle 200, the four cells cycled at 25°C showed almost identical values for the impedance rise whereas a significant capacity fade (see Fig. 9a) has already occurred. As the local distribution of reversible and irreversible thickness change presented in Figs. 6 and 7 indicates distinctly localized damaged areas, it is concluded that EIS at this high frequency is not capable to detect the observed inhomogeneities in enough detail for the cells studied in this work. Hence, the penetration depth of the excitation signal seems to be limited and its significance may assumed to be limited[62] for detecting local aging effects.

In Fig. 9d, the values for the cell impedance measured at 45 mHz showed a similar characteristic for all studied cells except for the cells cycled at a charging rate of 1 C at 25°C. At cycle 200, a significantly higher impedance was measured for cell #84 than for #83.

Comparing the values of the impedance rise in Fig. 9c and Fig. 9d of cell #83 and #84 at cycle 200, a significant deviation at 45 mHz for cell #84 appears which is missing at 1 kHz. At a low excitation frequency of 45 mHz, this impedance rise seems to be capable for detecting the already decreased capacity of the cell which is caused by the local damaged areas. Interestingly, the excitation frequency may have an influence on the quality of the gained EIS-data of the cell. Lower excitation frequency may increase the penetration depth and is therefore more suitable for detecting local damaging effects within the cell.[62]

The normalized irreversible thickness change is correlated to the impedance rise at 45 mHz in Fig. 10 and also to the normalized capacity fade in Fig. 11.

The irreversible thickness change in Fig. 10a shows an increased slope for both cells cycled at a charging rate of 1 C at 25°C compared to the remaining four which almost show identical characteristics (see Fig. 10b). At the second check-up after 100 cycles, the impedance rise for the four cells cycled at 25°C was determined to be around 5%, while the impedance increases for the cells cycled at 40°C were determined to be around 16%.

Comparing the four cells cycled at 25°C, the cells cycled at a charging rate of 1 C showed a greater thickness increase for nearly the same impedance rise compared to the ones cycled at a charging rate of 0.5 C. This coincides with the finding, that a certain capacity fade for the cells at 1 C occurred and hence the irreversible thickness change has already increased, which was already discussed in Figs. 9a and 9b. At 100 cycles, the temperature influence revealed in an higher value of the impedance for the cells cycled at 40°C compared to the cells cycled at 25°C. This phenomenon may be caused by temperature dependent aging effects like binder expansion,[63,64] enhanced SEI growth[10,48] or possible gas evolution.[54]

In Fig. 11a, the normalized irreversible thickness change and the capacity fade of all studied cells are shown. The normalized capacity fade (1-SOH) for the cells cycled at a charging rate of 1 C at 25°C was estimated to be around 30% and 40%, respectively. Regarding Fig. 11b, the cells at a charging rate of 0.5 C at 25°C were used in this aging test until 4.2% and the cells at 40°C until 6.4% of normalized capacity fade. Latter cells exhibited a steeper increase of irreversible thickness change at the same normalized capacity fade compared to the cells cycled at 25°C. A linear correlation (see Fig. 11a) can be approximated between the normalized capacity fade and the

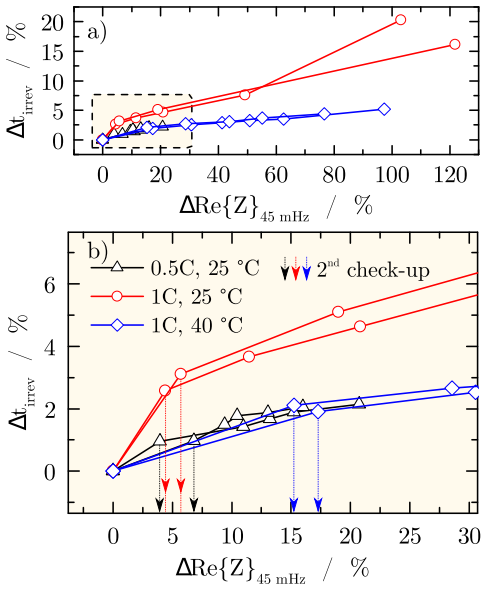

Figure 10. a) Normalized irreversible thickness increase and normalized impedance rise at 45 mHz. b) Magnified region marked in a) up to 7% irreversible thickness increase and 30% impedance rise. The range of the measured real parts at 45 mHz is depicted by the arrows referring to the second check-up after 100 cycles.

thickness increase for the cells cycled at a charging rate of 1 C at 25°C. This finding is confirmed by other researches which dealed with the correlation of stress increase during cyclic aging tests.[4] This phenomenon may indicate the continuous consumption of cycleable lithium due to the formation of deposited lithium on the surface of the active material. For the remaining cells the measured capacity fade in this study is too small for assuming a linear correlation.

The temperature influence on the relation between irreversible thickness change and capacity fade may be indicated by the steeper slope of the cell cycled at 40°C (see Fig. 11b). Enhanced SEI formation does not quite explain the increased slope as this process is regarded to consume lithium in the same amount and therefore no significant

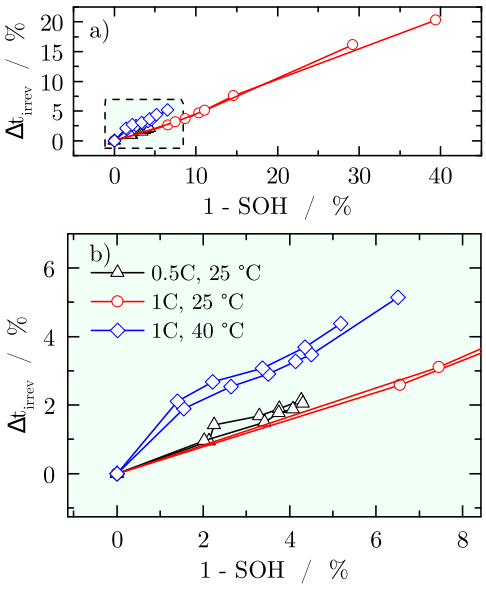

Figure 11. a) Normalized irreversible thickness increase correlated to normalized capacity fade (1-SOH) including all measurements. b) Magnified region marked in a) up to 7% normalized thickness increase and 8% capacity fade.

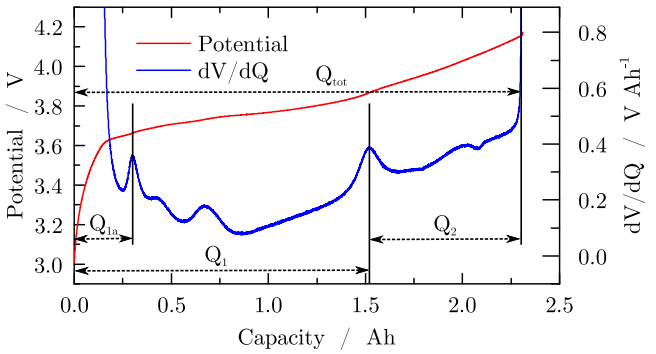

Figure 12. Cell potential V and its derivative $\frac{dV}{dQ}$ for cell #83 at a discharge rate of 1 C for cycle 0.

deviation for the slopes of all cells should be detectable.[11,65] Again, an explanation for this behavior may be additional gas evolution due to electrolyte decomposition[54] or binder degradation,[63,64,66] leading to a steeper electrode thickness increase and resistance rise at the same SOH. Since the cycling conditions included also different charging rates, a clear separation of temperature and charging rate induced effects cannot be conducted in this work and the authors assume, that the resulting characteristic is influenced by both effects at the same time.

Electrode specific capacity fade.—DVA according to the work of Keil et al.[31] was performed during the check-up to analyze the contributions of anode and cathode, respectively, to the overall capacity fade of the cell.[30] The results were compared to the displacement data in order to further elucidate the degradation mechanisms in this study. In Fig. 12 the measured cell potential and its derivative $\frac{dV}{dQ}$ related to the capacity of the cell is shown for cell #83 at cycle 0. Q_{tot} represents the total capacity of the cell. The part from zero up to Q_{1a} denotes the first graphite peak in the differential graphite potential at the transition from a lower Li loading to LiC_{12}. Q_1 represents the charge difference between the fully discharged state of the cell (SOC=0) and the central peak of the differential graphite potential at the transition of LiC_{12} to LiC_6. The remaining part Q_2 between Q_1 and Q_{tot} represents the distance between the fully charged state (SOC=1) and the central graphite peak and can be seen as an indicator for shifts in the electrode balancing which changes the total amount of cycleable lithium.[31]

The DVA analysis for all studied cell are shown in Fig. 13. For cells cycled at a charging rate of 1 C at 25°C (#83, #84) a significant

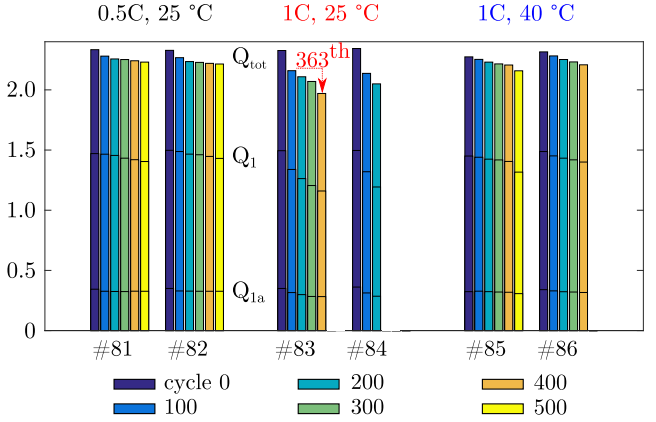

Figure 13. Differential voltage analysis (DVA) for all cells at all conducted check-ups. Cycling of cells #83 and #84 was stopped at cycle number 230 and 396, respectively, due to excessive capacity fade.

decrease of Q_1, while Q_2 stayed approximately constant, was derived from the check-ups at 0, 100 and 200 cycles, which points at a degradation mainly taking place within the anode. The authors assume that the greater part of the excessive capacity fade of the cell was caused by the degradation of the anode. This assumption is confirmed by the post-mortem analysis shown in Fig. 8 where deposit layers were only seen on the anode layers and no obvious degradation mechanism could be seen directly on the cathode layers. The DVA-analysis of the last check-ups at the 230th and 396th cycle, respectively, are missing in Fig. 13 because the peaks of the differential graphite potential could not be determined exactly for the highly degraded states of these cells (#83, #84).

The cells cycled at a charging rate of 0.5 C at 25°C and 1 C at 40°C showed a slightly decreasing capacity fade at higher cycle numbers which indicates that they were far from reaching their end of life.

Conclusions

Measuring the local thickness of lithium-ion pouch cells via laser-scanning was used to correlate reversible and irreversible thickness change to cell degradation during cyclic aging experiment. For cells showing a non-linear aging behavior, locally distributed damage was indicated by an initial reversible thickness change increase, followed by a decrease as soon as the irreversible thickness change increased dramatically within these cells. These effects were first seen in the area near the tabs and subsequently in the center of the cells, accompanied by excessive capacity fade. Post-mortem analysis and DVA-analysis revealed that the larger part of the cell degradation can be ascribed to the anode. The correlation of irreversible thickness increase, impedance rise and capacity fade provides helpful insights into the aging mechanisms of lithium-ion cells. But it also raises the question which mechanisms contribute to the irreversible thickness increase and to which extent, e.g. lithium plating, SEI formation, binder degradation or gas evolution. Further work will focus on the combination of thickness measurements with coulometric measurements and a more detailed investigation of the thermal influence on the aging behavior of lithium-ion cells. Overall, the presented method is a viable means of investigating dynamic thickness changes of lithium-ion cells and provides an interesting perspective on cell aging.

Acknowledgment

This project has received funding from the European Union's Horizon 2020 research and innovation program under grant agreement No. 713771.

References

1. B. Rieger, S. F. Schuster, S. V. Erhard, P. J. Osswald, A. Rheinfeld, C. Willmann, and A. Jossen, *Journal of Energy Storage*, **8**, 1 (2016).
2. X. M. Liu and C. B. Arnold, *Journal of The Electrochemical Society*, **163**, A2501 (2016).
3. T. Okoshi, K. Yamada, T. Hirasawa, and A. Emori, *Journal of Power Sources*, **158**, 874 (2006).
4. J. Cannarella and C. B. Arnold, *J. Power Sources*, **269**, 7 (2014).
5. B. Rieger, S. Schlueter, S. V. Erhard, J. Schmalz, G. Reinhart, and A. Jossen, *J. Energy Storage*, **6**, 213 (2016).
6. L. W. Sommer, A. Raghavan, P. Kiesel, B. Saha, J. Schwartz, A. Lochbaum, A. Ganguli, C.-J. Bae, and M. Alamgir, *J. Electrochem. Soc.*, **162**, A2664 (2015).
7. L. W. Sommer, P. Kiesel, A. Ganguli, A. Lochbaum, B. Saha, J. Schwartz, C.-J. Bae, M. Alamgir, and A. Raghavan, *J. Power Sources*, **296**, 46 (2015).
8. K.-Y. Oh, J. B. Siegel, L. Secondo, S. U. Kim, N. A. Samad, J. Qin, D. Anderson, K. Garikipati, A. Knobloch, B. I. Epureanu, C. W. Monroe, and A. Stefanopoulou, *J. Power Sources*, **267**, 197 (2014).
9. J. Cannarella and C. B. Arnold, *Journal of Power Sources*, **245**, 745 (2014).
10. M. B. Pinson and M. Z. Bazant, *Journal of the Electrochemical Society*, **160**, A243 (2012).
11. A. J. Smith, J. C. Burns, X. Zhao, D. Xiong, and J. R. Dahn, *Journal of The Electrochemical Society*, **158**, A447 (2011).
12. U. S. Kim, C. B. Shin, and C.-S. Kim, *Journal of Power Sources*, **180**, 909 (2008).
13. U. S. Kim, C. B. Shin, and C.-S. Kim, *Journal of Power Sources*, **189**, 841 (2009).
14. B. Wu, Z. Li, and J. Zhang, *Journal of the Electrochemical Society*, **162**, A181 (2014).
15. G.-H. Kim, K. Smith, K.-J. Lee, S. Santhanagopalan, and A. Pesaran, *Journal of The Electrochemical Society*, **158**, A955 (2011).
16. B. Bitzer and A. Gruhle, *J. Power Sources*, **262**, 297 (2014).
17. M. Klett, R. Eriksson, J. Groot, P. Svens, K. Ciosek Högström, R. W. Lindström, H. Berg, T. Gustafson, G. Lindbergh, and K. Edström, *Journal of Power Sources*, **257**, 126 (2014).
18. B. Markovsky, A. Rodkin, Y. Cohen, O. Palchik, E. Levi, D. Aurbach, H.-J. Kim, and M. Schmidt, *Journal of Power Sources*, **119–121**, 504 (2003).
19. K. Jalkanen, J. Karppinen, L. Skogström, T. Laurila, M. Nisula, and K. Vuorilehto, *Applied Energy*, **154**, 160 (2015).
20. A. Barai, G. H. Chouchelamane, Y. Guo, A. McGordon, and P. Jennings, *Journal of Power Sources*, **280**, 74 (2015).
21. S. Schindler, M. Bauer, M. Petzl, and M. A. Danzer, *J. Power Sources*, **304**, 170 (2016).
22. L. Cai, K. An, Z. Feng, C. Liang, and S. J. Harris, *J. Power Sources*, **236**, 163 (2013).
23. S. Shiotani, T. Naka, M. Morishima, M. Yonemura, T. Kamiyama, Y. Ishikawa, Y. Ukyo, Y. Uchimoto, and Z. Ogumi, *Journal of Power Sources*, **325**, 404 (2016).
24. V. Zinth, C. V. Lüders, M. Hofmann, J. Hattendorff, I. Buchberger, S. Erhard, J. Rebelo-Kornmeier, A. Jossen, and R. Gilles, *J. Power Sources*, **271**, 152 (2014).
25. S. C. Nagpure, B. Bhushan, and S. S. Babu, *Journal of the Electrochemical Society*, **160**, A2111 (2013).
26. B. Rieger, S. Schlueter, S. V. Erhard, and A. Jossen, *Journal of The Electrochemical Society*, **163**, A1595 (2016).
27. Z. J. Schiffer, J. Cannarella, and C. B. Arnold, *Journal of The Electrochemical Society*, **163**, A427 (2015).
28. C. Birkenmaier, B. Bitzer, M. Harzheim, A. Hintennach, and T. Schleid, *J. Electrochem. Soc.*, **162**, A2646 (2015).
29. S. F. Schuster, T. Bach, E. Fleder, J. Müller, M. Brand, G. Sextl, and A. Jossen, *J. Energy Storage*, **1**, 44 (2015).
30. P. Keil and A. Jossen, *Journal of The Electrochemical Society*, **164**, A6066 (2016).
31. P. Keil, S. F. Schuster, J. Wilhelm, J. Travi, A. Hauser, R. C. Karl, and A. Jossen, *Journal of The Electrochemical Society*, **163**, A1872 (2016).
32. K.-Y. Oh, B. I. Epureanu, J. B. Siegel, and A. G. Stefanopoulou, *J. Power Sources*, **310**, 118 (2016).
33. K.-Y. Oh and B. I. Epureanu, *J. Power Sources*, **303**, 86 (2016).
34. F. M. Kindermann, A. Noel, S. V. Erhard, and A. Jossen, *Electrochimica Acta*, **185**, 107 (2015).
35. M. Fleischhammer, T. Waldmann, G. Bisle, B.-I. Hogg, and M. Wohlfahrt-Mehrens, *J. Power Sources*, **274**, 432 (2015).
36. M. Tang, P. Albertus, and J. Newman, *J. Electrochem. Soc.*, **156**, A390 (2009).
37. V. A. Agubra, J. W. Fergus, R. Fu, and S.-Y. Choe, *J. Power Sources*, **270**, 213 (2014).
38. N. Zhang and H. Tang, *Journal of Power Sources*, **218**, 52 (2012).
39. R. S. Rubino, H. Gan, and E. S. Takeuchi, *Journal of The Electrochemical Society*, **148**, A1029 (2001).
40. K. Dai, Z. Wang, G. Ai, H. Zhao, W. Yuan, X. Song, V. Battaglia, C. Sun, K. Wu, and G. Liu, *Journal of Power Sources*, **298**, 349 (2015).
41. M. Petzl, M. Kasper, and M. A. Danzer, *J. Power Sources*, **275**, 799 (2015).
42. R. Mukherjee, A. V. Thomas, D. Datta, E. Singh, J. Li, O. Eksik, V. B. Shenoy, and N. Koratkar, *Nat Comms*, **5** (2014).
43. V. A. Agubra, J. W. Fergus, R. Fu, and S.-Y. Choe, *Electrochim. Acta*, **149**, 1 (2014).
44. T. Waldmann, M. Kasper, and M. Wohlfahrt-Mehrens, *Electrochimica Acta*, **178**, 525 (2015).
45. D. Burow, K. Sergeeva, S. Calles, K. Schorb, A. Börger, C. Roth, and P. Heitjans, *Journal of Power Sources*, **307**, 806 (2016).
46. U. Tröltzsch, O. Kanoun, and H.-R. Tränkler, *Electrochimica Acta*, **51**, 1664 (2006).
47. T. C. Bach, S. F. Schuster, E. Fleder, J. Müller, M. J. Brand, H. Lorrmann, A. Jossen, and G. Sextl, *J. Energy Storage* (2016).
48. I. Buchberger, S. Seidlmayer, A. Pokharel, M. Piana, J. Hattendorff, P. Kudejova, R. Gilles, and H. A. Gasteiger, *J. Electrochem. Soc.*, **162**, A2737 (2015).
49. S. Mohan, Y. Kim, J. B. Siegel, N. A. Samad, and A. G. Stefanopoulou, *Journal of the Electrochemical Society*, **161**, A2222 (2014).
50. N. A. Samad, Y. Kim, J. B. Siegel, and A. G. Stefanopoulou, *Journal of The Electrochemical Society*, **163**, A1584 (2016).
51. J. H. Lee, H. M. Lee, and S. Ahn, *Journal of Power Sources*, **119–121**, 833 (2003).
52. A. Mukhopadhyay, A. Tokranov, X. Xiao, and B. W. Sheldon, *Electrochimica Acta*, **66**, 28 (2012).
53. D. Liu, Y. Wang, Y. Xie, L. He, J. Chen, K. Wu, R. Xu, and Y. Gao, *Journal of Power Sources*, **232**, 29 (2013).
54. B. B. Berkes, A. Jozwiuk, H. Sommer, T. Brezesinski, and J. Janek, *Electrochemistry Communications*, **60**, 64 (2015).
55. G. Zhang, C. E. Shaffer, C.-Y. Wang, and C. D. Rahn, *Journal of the Electrochemical Society*, **160**, A610 (2013).
56. B. V. Ratnakumar and M. C. Smart, *ECS Transactions*, **25**, 241 (2010).
57. W. Lu, C. M. López, N. Liu, J. T. Vaughey, A. Jansen, and D. W. Dees, *Journal of The Electrochemical Society* , **159**, A566 (2012).
58. S. Smiles and R. O. Herzog, *Chemische Konstitution und Physikalische Eigenschaften*; Springer Berlin Heidelberg and Imprint and Springer: Berlin, Heidelberg, 1914.
59. C.-Y. Tang and S. J. Dillon, *Journal of The Electrochemical Society*, **163**, A1660 (2016).
60. K. G. Gallagher, S. E. Trask, C. Bauer, T. Woehrle, S. F. Lux, M. Tschech, P. Lamp, B. J. Polzin, S. Ha, B. Long, Q. Wu, W. Lu, D. W. Dees, and A. N. Jansen, *Journal of The Electrochemical Society*, **163**, A138 (2015).
61. Y. Xie, J. Li, and C. Yuan, *Journal of Power Sources*, **248**, 172 (2014).

62. P. J. Osswald, S. V. Erhard, A. Noel, P. Keil, F. M. Kindermann, H. Hoster, and A. Jossen, *Journal of Power Sources*, **314**, 93 (2016).
63. Z. Zhang, T. Zeng, Y. Lai, M. Jia, and J. Li, *Journal of Power Sources*, **247**, 1 (2014).
64. W. Wu, X. Xiao, M. Wang, and X. Huang, *Journal of the Electrochemical Society*, **161**, A803 (2014).
65. T. Bond, J. Zhou, and J. Cutler, *Journal of The Electrochemical Society*, **164**, A6158 (2016).
66. E. K. Rahani and V. B. Shenoy, *Journal of the Electrochemical Society*, **160**, A1153 (2013).
67. B. Rieger, S. V. Erhard, K. Rumpf, and A. Jossen, *J. Electrochem. Soc.*, **163**, A1566 (2016).